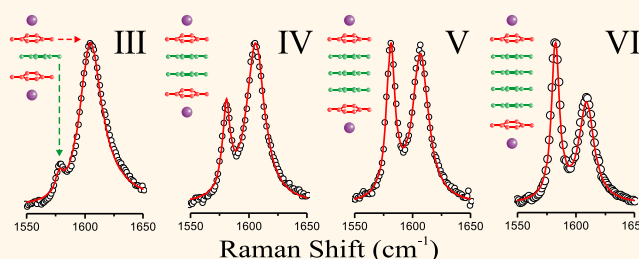


Manifestation of Charged and Strained Graphene Layers in the Raman Response of Graphite Intercalation Compounds

Julio C. Chacón-Torres,[†] Ludger Wirtz,^{‡,¶} and Thomas Pichler^{†,*}

[†]Faculty of Physics, University of Vienna, Strudlhofgasse 4, A-1090 Vienna, Austria, [‡]Physics and Materials Science Research Unit, University of Luxembourg, Campus Limpertsberg, L-1511 Luxembourg, Luxembourg, and [¶]Institute for Electronics, Microelectronics, and Nanotechnology (IEMN), CNRS-UMR 8520, Dept. ISEN, 59652 Villeneuve d'Ascq, France

ABSTRACT We present detailed multifrequency resonant Raman measurements of potassium graphite intercalation compounds (GICs). From a well-controlled and consecutive *in situ* intercalation and high-temperature deintercalation approach the response of each stage up to stage VI is identified. The positions of the G and 2D lines as a function of staging depend on the charge transfer from K to the graphite layers and on the lattice expansion. *Ab initio* calculations of the density and the electronic band structure demonstrate



that most (but not all) of the transferred charge remains on the graphene sheets adjacent to the intercalant layers. This leads to an electronic decoupling of these "outer" layers from the ones sandwiched between carbon layers and consequently to a decoupling of the corresponding Raman spectra. Thus, higher stage GICs offer the possibility to measure the vibrations of single, double, and multilayer graphene under conditions of biaxial strain. This strain can additionally be correlated to the in-plane lattice constants of GICs determined by X-ray diffraction. The outcome of this study demonstrates that Raman spectroscopy is a very powerful tool to identify local internal strain in pristine and weakly charged single and few-layer graphene and their composites, yielding even absolute lattice constants.

KEYWORDS: graphite intercalation compounds · graphene · Raman spectroscopy · charge transfer · strain determination

Raman spectroscopy is a key tool to probe the physical and electronic properties in graphene-based materials.^{1–4} Analysis of the two main signals in the Raman spectra, the so-called G-line around 1582 cm^{−1} and the dispersive double-resonance peak in the range between 2600 and 2700 cm^{−1} (which carries both the name G' line and 2D line in the literature), offers detailed information; e.g., it allows determination of the number of graphene layers,^{2,5} induced strain in the structure,^{6–9} and charging.^{10–13} We show in this report how layer stacking, strain, and charging influence in detail the Raman spectra of graphite intercalation compounds.

Graphite intercalation compounds (GICs) consist of a consecutive stacking of graphene layers with intercalated alkali metals, alkali earth metals, or rare-earth elements as well as p-type dopands like FeCl₃, AsF₅, or H₂SO₄ in between.^{14–21} GICs are classified in stages I, II, III, ..., *n* where stage *n* means that

one intercalant layer follows after *n* (usually AB stacked) graphene layers. The electronic band structure, charge transfer of different alkali stage I GICs, was also directly measured by photoemission spectroscopy^{22,23} and recently with more accuracy for the full Fermi surface, quasiparticle band structure, and Dirac cone in KC₈.^{24,25} The influence of the charge transfer on the electronic structure and optical properties was studied using *ab initio*²⁶ and tight-binding calculations^{27,28} for n- and p-type intercalation at high staging. Combination of the reflectivity spectra of alkali GIC up to stage IV with such calculation revealed a good agreement.¹⁶

The structural characterization of the different GICs is based on X-ray diffraction (XRD) and has revealed a linear in-plane lattice expansion²⁹ as a function of inverse stage for stages III–VI. Later, a combination of Raman spectroscopy and XRD^{30,31} was used to assign and analyze the vibronic structure for stage I to stage VI in alkali GICs.

* Address correspondence to thomas.pichler@univie.ac.at.

Received for review July 26, 2013 and accepted September 11, 2013.

Published online September 11, 2013
10.1021/nn403885k

© 2013 American Chemical Society

Beyond stage III, one can distinguish between “outer” graphene layers that are adjacent to an intercalant layer which are usually heavily charged and referred to as bounding layer in the literature and the “inner” layers that carry very little charge and are referred to as interior layers in the literature. To highlight the importance of the charge transfer, we will refer to them in the following as charged (c) and uncharged (uc) layers. This nearest layer (NL) model was invoked in order to explain the splitting of the G line for alkali GICs of stage III and higher.³¹ The lower frequency G-line at about 1580 cm^{-1} corresponds in position to the G-line of neutral graphite and was therefore ascribed to the uc layers (supported by the fact that it is absent in stage I and stage II GICs). The higher frequency line at about 1610 cm^{-1} , which is present for all stages, was consequently ascribed to the c layers, even though the exact mechanism of the stiffening remained unclear at the time. The stiffening has by now been understood as the effect of nonadiabaticity onto the vibrations of charged graphene layers³² and *ab initio* calculations of stage I GICs have indeed confirmed the strong blue-shift of the G-line.³³ The NL model has been successful in identifying the different stages through the relative intensities of the G-lines of uc and c layers. However, the model alone is not able to explain the subtle frequency shifts of the G-line for the different stages and has not yet been used to investigate the dependence of the 2D line on staging.

In this report, we present an extensive Raman spectroscopy study of potassium GICs, measuring both the G and the 2D lines for different laser energies and for the different intercalation stages up to stage VI. The measurements are accompanied by *ab initio* calculations of the electronic structure, charge transfer, lattice expansion, and vibrational properties of these GICs. We present a quantitative refinement of the nearest layer

model which takes into account the exact charge transfer, the lattice expansion, and the effect of AB-stacking of the inner (uc) layers. By comparing our results with the available experimental data on charged, strained, and multistacked graphene layers, we show how to disentangle the different (partially counteracting) effects onto the position of the Raman lines. We will show that this has important implications for the application of Raman spectroscopy to identify, for instance, the strain in nanocarbon-based nanoelectronic and optoelectronic devices as well as the local interfacial strain in graphene and carbon nanotube polymer composites on an absolute scale.

RESULTS AND DISCUSSION

Raman Response of Stage II to Stage VI GICs. We consider KC_8 as our starting potassium–graphite intercalation phase. Then we performed controlled temperature-driven deintercalation experiments to synthesize the higher intercalation stages: stage II (KC_{24}), stage III (KC_{36}), stage IV (KC_{48}), stage V (KC_{60}), and stage VI (KC_{72}). The corresponding Raman spectra recorded with a 568 nm laser excitation are depicted in Figure 1 (a). The G-line always displays a high frequency component G_c between 1600 and 1610 cm^{-1} . This mode has a slight asymmetry due to the Fano interference of the conduction electrons in the electron-doped charged layers, and it is related to the charged graphene layers next to an intercalant layer. This assignment is also confirmed by comparison to stage II KC_{24} , where each graphene layer is in contact with potassium atoms and only charged graphene layers exist. Hence, KC_{24} exhibits only one G-line as G_c at 1610 cm^{-1} . In addition, for stages higher than KC_{24} a second line G_{uc} appears around 1580 cm^{-1} . The position of the G_{uc} is close to the G-line in pristine graphite (1583 cm^{-1}) and of graphene³⁴ (1580 cm^{-1}). Therefore, G_{uc} is assigned to

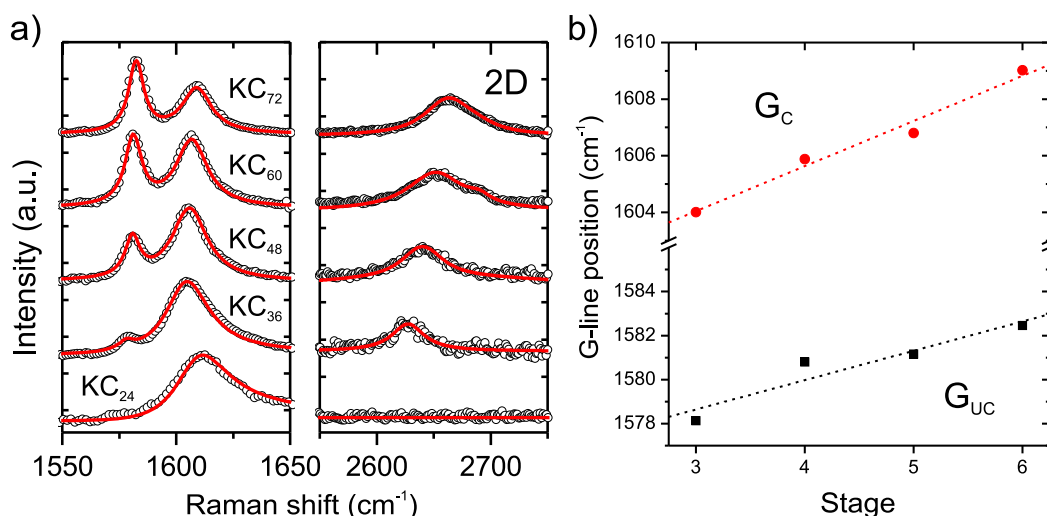


Figure 1. Raman spectra of stage II to VI GIC measured with a laser wavelength of 568 nm. Panel (a): spectra (black dots) together with the results of a line shape analysis (red line) in the region of the G and 2D line are depicted. Panel (b): positions of the two G-line components (G_c and G_{uc} as a function of stage n).

the response of basically uncharged graphene layers surrounded by charged graphene layers. A detailed line shape analysis of the two G-line components using an asymmetric Fano line for the charged layers (G_c) next to an intercalant layer and a Lorentzian line for the uncharged carbon layers (G_{uc}) was performed. The results closely match the experimental spectra and are depicted as solid lines in Figure 1 (a). As shown in Figure 1 (b), the positions of these two components are not constant and have a linear dependence on the intercalation stage. This shift is not predicted by the NL model. We will explain the shift below in an analysis that takes into account the small fractional charging even of the inner layers and the lattice expansion due to intercalation.

We find a linear relation between the intensity ratio $R = I_{uc}/I_c$ of the two G-line components (G_{uc} and G_c), in agreement with the NL model. Our results using the 568 nm laser excitation agree very well with the results of Solin et al.³¹ R is also independent from the type of alkali metal intercalant for the case of K, Rb, and Cs GICs.³¹ In order to analyze these highly staged GICs in more detail we performed a complete multifrequency analysis (see also Figures 1 and 2 in the Supporting Information). A clear photon energy dependence of the intensity ratio between the charged and uncharged G-line components is observed, but the linear dependence of R is universal and can be safely used for the identification of the different stages (following the protocol explained below in the methods). This shows that in all cases the predominant charge transfer from the intercalant to the neighboring graphene layer is a valid approximation. The different slopes for different photon energies can be tentatively explained by a different frequency-dependent resonance Raman cross section of G_c and G_{uc} and by different charge carrier absorption of the charged layers at high photon energies. This means that, in agreement with previous results, Raman spectroscopy can be used to unambiguously identify the different stages and correlate them to structural assignments by XRD.

We now turn to a detailed analysis of the double-resonant 2D line. The NL model lets us expect that c and uc graphene layers give rise to separate 2D lines. We observe experimentally that the 2D-line is absent for stage I and stage II potassium GICs but present for the higher order stages and for pure graphene and graphite. This means that the 2D response is only due to the inner (uc) layers. The double resonance is suppressed for the outer (c) layers due to the strong charging. Therefore, in stage I and stage II GICs where all graphene layers are adjacent to an intercalant, the 2D line is suppressed altogether. Interestingly, this is not the case for p-type intercalation as demonstrated by recent results on $FeCl_3$ -doped multilayer graphene, owing to a doping level similar to stage I GIC.²⁰ This different behavior might be due to a different localization of the charges transferred to the $FeCl_3$ ions upon

p-type doping, which should be investigated in future studies. For the potassium intercalation stages III–VI, the 2D line displays a clear dispersion with respect to the laser energy and possesses a fine structure that depends on the number of uc layers (see Figure 2 (b)).

Considering that the double-resonant Raman peak arises from the inner graphene layers only, we can regard the inner layer of KC_{36} as a graphene monolayer, the inner two layers of KC_{48} as a bilayer, the inner three layers of KC_{60} as a trilayer, and the four inner layers in KC_{72} as a quadrilayer graphene. In the analysis, we can thus draw an analogy with the splitting of the 2D-line in double- and few-layer graphene.^{1,5} A closer inspection of the 2D-line of the different GIC stages and fitting with two Voigtian functions demonstrates indeed a splitting of this line starting with stage IV (see Figure 2 (b)). We observe a splitting of 25.71, 38.34, and 39.48 cm^{-1} between the two Voigtian functions of stage IV, stage V, and stage VI, respectively, while stage III presents a 2D-line with one component only. In Figure 2 (a), we display the dispersion of the 2D line as a function of the laser energy. For the stages where the 2D-line split, we use the position of the lower frequency peak which is much more intense than the upper frequency peak as it can be seen in panel (b) of Figure 2 and as it has been explained in ref 37. The slope of the 2D dispersion as a function of the laser energy is about 99 cm^{-1}/eV for all of the different stages. This agrees with the dispersion of the 2D line of natural graphite, turbostratic graphite,¹⁰ and graphene/Si,³⁸ which are also shown in Figure 2 (a). We point out that the 2D response of bilayer graphene splits in four components,³⁸ but due to the low intensity of two of the components, these features were not resolvable in the 2D spectra of KC_{48} . Therefore, we used the two main components as a good approximation for the line position in the 2D response and found a good agreement in the dispersion.

However, the actual position of the 2D line depends on the stage of the GIC, e.g., the 2D line of the inner layer in KC_{36} is down-shifted by about $\sim 36\text{ cm}^{-1}$ as compared to the 2D line of pristine graphene. Similarly, the 2D lines of KC_{48} , KC_{60} , KC_{72} are downshifted with respect to those of bi-, tri-, and quadri-layer graphene, respectively. The amount of the downshift decreases with higher stage number. In order to explore all possible reasons for this very pronounced down shift, we have performed a detailed theoretical analysis based on *ab initio* calculations of charge density, electronic dispersion, and phonon frequencies.

Theoretical Discussion of the Raman Spectra. We discuss first the amount of charge transfer from the potassium intercalant layer to the different graphene layers. For this purpose, we have calculated the total charge density $\rho_{GIC}(z)$ as a function of the direction perpendicular to the layers, averaged over the in-plane directions (x – y plane). From this, we subtract the

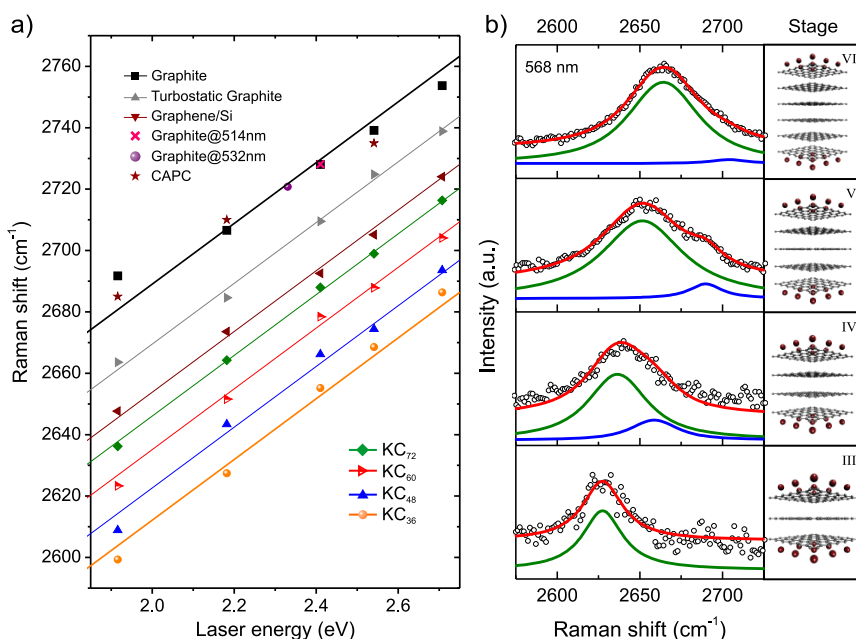


Figure 2. (a) Dispersion of the most intense double-resonant 2D Raman mode in GIC, graphite and graphenes as function of laser energy. The different symbols depict the experimental 2D-line position measured. The values of graphene/Si, turbostatic graphite, and pristine graphite were extracted from refs 10 and 5, 11, and 35, respectively. For comparison, the 2D-line position of graphite at 514 and 532 nm (refs 2 and 34) are depicted as well as compression annealed pyrolytic carbon (CAPC) which falls into the same graphitic slope.³⁶ (b) Detailed line-shape analysis of the 2D-line in stages III–VI is shown using up to two Voightians (green and blue lines). The result of the analysis is shown as a red line.

"reference charge density", $\rho_{\text{ref}}(z) = \rho_{\text{C}}(z) + \rho_{\text{K}}$ which is the sum of the charge densities of the graphene layers and potassium layers calculated separately (in the geometry of the compound system). This method follows the earlier calculations by Hartwigsen et al.³⁹ on stage I intercalation compounds and by Ancilotto and Toigo⁴⁰ on potassium adsorbed on a graphite surface. The charge density difference, $\Delta\rho(z) = \rho_{\text{GIC}}(z) - \rho_{\text{ref}}(z)$, is thus a convenient quantity to visualize charge transfer: it is negative around the position of the K atoms which tend to donate their electrons and it is positive where those electrons are accumulated. Figure 3 (a) demonstrates this for stage III KC₃₆ under ABA-stacking, and stage VI KC₇₂ under AAA-stacking is shown in Figure 3 (c) (approximated model). Obviously, the electrons donated by the potassium atoms accumulate mainly on the potassium boundary carbon layers. In order to calculate a value for the charge transfer, we define (somewhat arbitrarily) the limit between the potassium and the carbon layer (marked z' in Figure 3 (a and c) as the value of z where $\Delta\rho(z)$ changes sign. Integrating the density-difference curve between those limits, one obtains a charge transfer of 0.39 electrons from each potassium atom to the graphene layers. Table 1 contains detailed information on the charge accumulation per layer. Most of the transferred electrons accumulate on the outer graphene layer. The charge concentration on this layer is almost independent of the staging. In contrast, the charge concentration on the inner

layers remains (relatively) low and varies with the stage number.

This explains why both the G_{C} and G_{UC} components depend only weakly on the stage number. The splitting which was already observed by Solin and Caswell³¹ can now be understood on the basis of the high (and constant) charge density of the charged graphene layers. Due to the breakdown of the Born–Oppenheimer expansion, charging of graphene leads to a strong stiffening of the G-mode.³² By electrochemical top-gating, electron concentrations of up to $5 \times 10^{13}/\text{cm}^2$ have been achieved,⁴¹ leading to a G-line position at about 1605 cm^{-1} . In GICs, the charge density on the G_{C} component reaches similar values (see Table 1), which explains its high frequency. On the other hand, the low frequency observed for the uncharged component G_{UC} is also slightly affected by this charge transfer beyond the nearest neighbor. We obtained the G-line upshift due to the charge density by using σ from Table 1, and eq 3 from ref 42 as it gives the response of the system under adiabatic+expanded lattice conditions. This yields a calculated G_{UC} of between 1584 cm^{-1} and 1586 cm^{-1} for all different GICs. This is strongly overestimating the observed values and even yields the wrong trend, which highlights that there is some important ingredient missing in our explanation.

In order to address this point, we first turn to the discussion of the 2D-line as a function of staging, making use of the double-resonance Raman model of Thomsen and Reich.⁴³ The model successfully

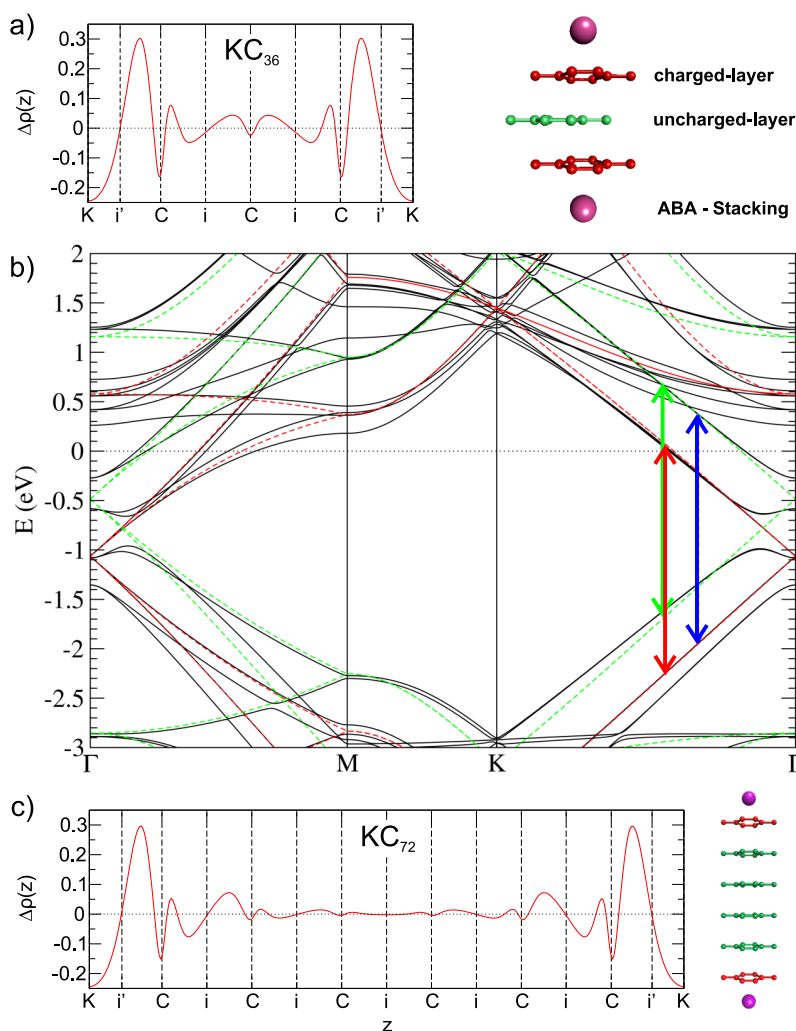


Figure 3. Charge density and band structure analysis. (a) Charge density distribution for KC_{36} with a sketch of the charged and uncharged layers. In the charge density analysis, the position of planes consisting of carbon/potassium atoms is marked by C/K, respectively. Midpoints between graphene planes are marked by i , and separation of the K and C planes, defined as the position where the density difference crosses 0, is marked by i' . (b) Band structure of KC_{36} (black solid lines) and of pure graphene from our *ab initio* calculations is shown. The pristine graphene bands are shifted in energy to match the bands of the charged layer (red dashed lines) and of the uncharged layer (green dashed lines). The red, green, and blue vertical arrows mark the transition between the π -bands of the charged–charged, uncharged–uncharged, and charged–uncharged layers at 2.3 eV laser energy. (c) Same analysis of the charge distribution as in (a) is depicted for KC_{72} .

TABLE 1. Calculated Charge Transfer (e^- per K atoms) from the Intercalated K Atoms to the Graphene Layers for Stage III–VI Potassium GIC^a

	el per K atom				σ ($10^{13}/\text{cm}^2$) ^b			
	<i>K</i>	first	second	third	first	second	third	biaxial strain (%)
KC ₃₆	−0.39	0.33	0.12		5.2	1.9		0.20
KC ₄₈	−0.39	0.28	0.11		4.5	1.7		0.13
KC ₆₀	−0.39	0.26	0.11	0.04	4.1	1.7	0.6	0.10
KC ₇₂	−0.39	0.26	0.10	0.03	4.1	1.6	0.5	0.06

^aThe last column gives the biaxial strain of the graphene layers.²⁹ ^bThe corresponding electron density is given in electrons/ cm^2 .

describes the D and 2D dispersion as a function of laser energy as well as the splitting of the 2D line for double, triple, and multilayer graphene,^{1,5} provided

that renormalization of the highest optical-phonon branch (HOB) due to electron-correlation effects is properly taken into account.⁴⁴ The different intercalation stages (second, third, fourth, etc.) can be viewed, respectively, as bi-, tri-, and quadrilayer graphene, separated by K intercalant layers. One might thus expect a similar splitting and shifting of the 2D line as observed in refs 1 and 5. Instead, the experiments show an absence of the 2D-line for the stage II GIC, a single 2D-line for the stage III compound and an upshift of the 2D line with increasing staging order (see Figure 2). This difference can be understood as due to the charging of the graphene layers adjacent to the K atoms. In order to demonstrate this, we show in Figure 3 (b) the electronic band-structure (DFT-LDA) of stage III GIC KC_{36} (in ABA-stacking configuration). The unit-cell contains 24 atoms per carbon layer; thus, the

band-structure is plotted in a $2\sqrt{3} \times 2\sqrt{3}$ supercell (compared to the primitive cell of graphene that contains only 2 atoms). In this supercell, the high-symmetry point K of the Brillouin zone of graphene is folded back onto Γ .

KC₃₆ displays notable exceptions from the linear crossing of the π -bands due to the interlayer interaction. Along with the band structure of GIC, we plot the band structure of pure graphene, displaying the linear crossing of the π -bands at Γ (K in the primitive cell). We shift the graphene bands in energy such that they match the corresponding bands of KC₃₆. The red-dashed lines correspond to the electronic bands of the charged graphene layers. The Dirac point is shifted to $\Delta E_1 = 1.07$ eV below the Fermi level, corresponding to a strong charging.

The green-dashed lines correspond to the electronic states of the weakly charged layer. Correspondingly, the Dirac point is shifted downward only by $\Delta E_2 = 0.49$ eV. This shift of the Dirac point gives us an additional measure for the charge density of the layers: From the density of states of graphene, $n(E) = |E|/(\pi\hbar^2v^2)$, where v is the Fermi velocity of graphene, one obtains the charge density by integration over the energy from the Dirac point to the Fermi level: $\sigma(E_F) = ((E_F)^2e)/(2\pi\hbar^2v^2)$. This connection of Fermi-level shift and electron density was also used in ref 45 for the determination of the average doping level based on work-function measurements.

With the DFT–LDA value of the Fermi velocity of $v = 0.85 \times 10^6$ m/s,⁴⁶ we obtain $\sigma_1 = 5.9 \times 10^{13}$ cm^{−2} for the charged layer and $\sigma_2 = 1.2 \times 10^{13}$ cm^{−2} for the uncharged layer in KC₃₆ (Figure 3 a). The value of σ_1 is 13% larger than the corresponding value in Table 1, while the value of σ_2 is 47% smaller than the value in Table 1. These differences give an indication of the uncertainties of different charge-transfer assignments (the electrons localized in between layers cannot be unambiguously assigned as belonging to one or the other layer). We note that our band-structure calculation is in qualitative agreement with the early *ab initio* band-structure calculations of Ohno and Kimamura.²⁶ The difference is that in the present work the fractional charge transfer from the intercalant layer to the graphene layers is calculated self-consistently while in ref 26 it was introduced as a parameter.

Concerning the 2D-line results of KC₃₆, we need to answer two questions: (i) Why is the 2D-line not split into two peaks like the G-line? (ii) Why is the 2D line downshifted by about 40 cm^{−1} compared to pure graphene?

In Figure 3 (b), vertical arrows mark dipole-allowed electron–hole pair transitions corresponding to a laser energy of 2.3 eV. Since in this energy range, the π -bands of KC₃₆ almost exactly match the (shifted) π -bands of pure graphene, the transitions take place at the same electronic wave-vector. In the double-resonance Raman model the electron/hole performs

a quasi-horizontal transition to a state in the vicinity of the neighboring point K'. This means that phonons with equal wave-vector \mathbf{q} are excited in graphene and KC₃₆. The red vertical arrow marks a transition where the excited electron is barely above the Fermi level. This transition (in the charged layer) is therefore strongly suppressed with respect to the one marked by the green vertical arrow which is an electronic excitation in the uncharged layer. Thus, contrary to the G-line, only one component of the 2D-line is present in the spectrum of KC₃₆ (and no 2D-line is visible for stage II GIC KC₂₄ where only the strongly charged layers exist).

We have also considered the blue vertical transition from the π -band of the charged layer to the π^* band of the uncharged layer. However, since it is an interlayer transition, its oscillator strength is negligible compared to that of the intralayer excitations. Since the electronic structure of the uncharged layer is decoupled from that of the charged layer (as manifested by the almost rigid band shift in Figure 3 b), one might expect little or no difference in frequency between the 2D line of isolated graphene and the one of KC₃₆. Indeed, several reasons could be found (related to the strong Kohn anomaly of the highest-optical branch at K⁴⁷) that could even explain a slight upshift of the 2D-line: (i) The residual charging of the inner layer leads to a reduction of the electron–phonon coupling around K⁴⁸ and might increase the 2D position by 10 cm^{−1} (extrapolated from Figure 2 (d) of ref 13). (ii) The opening of a gap between the π bands at Γ (K) could lead to a partial suppression of the Kohn anomaly in analogy to what happens to graphene in close contact with a Ni(111) surface.⁴⁹ (iii) The dielectric screening by the quasi-metallic environment could reduce the Kohn anomaly as recently observed for graphene on dielectric substrates.⁵⁰ In order to check if any of the above three arguments holds, we performed a phonon calculation (see Materials and Methods section) of the HOB (highest optical-phonon branch) at K, comparing the mode of the single layer with the mode of the inner layer of stage III potassium GIC. The mode of the uncharged layer has a frequency of 1269.6 cm^{−1}, while the mode of the single layer has 1271.9 cm^{−1}. We conclude that the phonons of the HOB around K remain essentially unchanged if the lattice constant of KC₃₆ is the same as the one of graphene. However, there are subtle changes for the lattice constant as a function of staging. Nixon and Parry have measured the expansion of the carbon–carbon bond length in potassium GIC (see Table 4 in ref 29). The lattice constant of KC₃₆ is 0.20% larger than the one of graphite. In order to verify this experimental result, we have performed a full cell-optimization of KC₃₆ and of pure graphite: we obtain a theoretical bond-length expansion of $\sim 0.22\%$ in very good agreement with the experiments.

Therefore, we can use the experimental lattice expansion from the XRD measurements in ref 29 of different GICs (whose values are also given as last column in Table 1) to evaluate the redshift of the Raman response. This is equivalent to putting strain on the individual graphene layers. This strain-induced lattice expansion in graphene has previously been related to the phonon frequency of the G and 2D line using the Grüneisen parameter^{2,8} in experiments applying uniaxial^{5,7,9} and biaxial strain.⁸ In our experiments, the regular incorporation of potassium atoms in between the layered structure of graphite, results in biaxial strained graphene layers. The shift of Raman frequency as function of strain was calculated by using the relation $\gamma = -1/\omega_0 \cdot \partial\omega/\partial\epsilon$ where ω_0 is the Raman frequency without strain, $\partial\epsilon$ is our calculated biaxial strain in GIC, and $\gamma = 2.2$ and 3.3 is the Grüneisen parameter for the G and 2D band phonons, respectively.⁸

For KC₃₆ we have calculated the phonon-frequency shift of pristine graphene and lattice-expanded graphene. For the HOB between K and M the frequency down-shift is about 18 cm^{-1} . This corresponds to a 2D-line redshift by 36 cm^{-1} . Thus, we can conclude that the redshift of the 2D-line (with respect to graphene) is almost entirely due to the small (but non-negligible) lattice expansion of the GIC. This lattice expansion also has a profound influence on the G-line position. This latter is, however, also influenced by the charge transfer as will be described in detail below.

Charge Transfer and Biaxially Strained Graphene Layers in GIC. These two factors had been linked by Pietronero and Strässler⁵¹ considering the well-established C–C bond length in GIC as a main tool to determine the charge transfer in those systems. Hitherto, these two main factors directly affect the Raman response in GIC by (i) the induced charge transferred from the K atoms into the carbon layers and (ii) the in-plane strain coming from the change in the C–C bond length. However, no detailed quantitative information about this strain nor about its origin in the case of donor compounds is known to date. Our analysis about the charge transfer and biaxial strain has revealed not only the fractional charge transfer per intercalant atom (Table 1) but also a solid understanding of its relationship with the electronic band structures of the GICs (Figure 3 (b)) and their corresponding Raman spectrum as it will be explained in the following and depicted in Figure 4.

In the left panel (Figure 4 (a)), we show the frequency dependence of the G-line components as a function of inverse stage. Experimentally, for both the G_{uc} and the G_c component (red circles), we observe a linear decrease in frequency from stage VI to III. The slope as a function of inverse stage (red dashed line) is slightly lower for G_{uc}. In addition, the C–C bond length of the different GIC from XRD studies of the in-plane

lattice expansion of ref 29 are shown on the top axis. In order to understand the staging dependence of both G-line components, we have to add the effect of lattice expansion and of charge transfer. Starting from the G-line position of pristine graphene^{1,34} (black dashed line), we have to add the upshift from the increased charge density on the layers and the down shift from the biaxial strain on the graphene layers and the corresponding change in the C–C bond length. We show these two contributions to the G-line as vertical green arrows (for the charge transfer related stiffening including the corresponding lattice expansion⁴²) and vertical blue arrows (for the additional effective biaxial strain), respectively. For the G_{uc} component we can evaluate the upshift due to the increased charge density using our calculated charge transfer to the G_{uc} summarized in Table 1 (green open circles in Figure 4 (a)). The resulting charge transfer to the G_{uc} is lowest for KC₇₂ and has an approximately linear increase with inverse stage. Concomitantly, the downshift due to the effective biaxial strain (blue open circles) are also shown. The resulting frequencies of the G_{uc} component in GIC (blue crosses) perfectly match the values of the experimental G_{uc}. In order to confirm the additivity of the effects of charge transfer and lattice expansion, we also performed nonadiabatic calculations of the phonon frequency of charged layers a fixed lattice constant. For this purpose, we use the method for the nonadiabatic phonon calculation of ref 52, which yields values very close to the method of ref 42. For KC₃₆ this yields a nominal upshift of 13.8 cm^{-1} for the G_{uc}, which together with the downshift of 15 cm^{-1} (determined from the experimental total lattice expansion determined by XRD using the Grüneisen parameter for the G phonons of ref 8), yields a position of 1579.6 cm^{-1} . This is in excellent agreement with the results using an effective strain. We also verified computationally (by variation of the lattice constant for neutral and charged graphene) that the Grüneisen parameter remains constant for the charge values observed in GICs. This means that both effects are truly additive. For the G_{uc}, about 50% of the observed experimental average lattice expansion measured by XRD are related to the charge transfer from the intercalants.

For the highly doped G_c component the story is more complex. Experimentally, the Raman response of highly doped graphene has been achieved by polymer electrolyte gating^{41,53} and by alkali metal vapor dosing.^{17,54} Interestingly, for a broad range of electron concentrations between $4 \times 10^{13}/\text{cm}^{-2}$ and $10 \times 10^{13}/\text{cm}^{-2}$ a position of 1611 cm^{-1} , very similar to the 1610 cm^{-1} mode in highly charged KC₂₄, is observed.⁵⁴ This saturation in the Raman frequency at high doping is also reported theoretically,⁴² although the absolute frequency is not correctly addressed in the theoretical description at high charge transfer. Therefore, in a

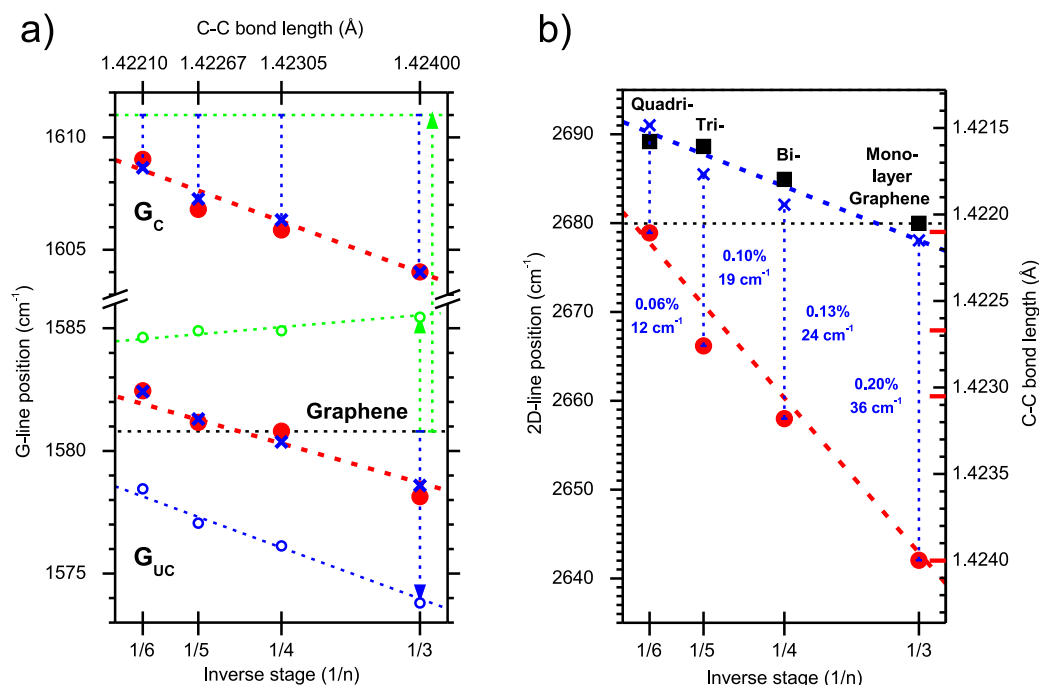


Figure 4. (a) G-lines of the potassium GIC depicted as a function of the inverse stage. The upper x-scale depicts the C—C bond length of the XRD results of ref29. The dashed green lines and the green open circles show the G-line upshift due to the high charge transfer to the charged G_C component and the remaining small charge transfer to the G_{UC} component. The blue dashed line and blue open circles come from the biaxial strain induced softening of the G-line of graphene (black dashed line). The blue crosses depict the positions after adding the charge transfer and subtracting the internal strain. (b) 2D-line position of the high-frequency-mode of GIC (red circles) and of unstrained (multilayer)graphenes from ref5 (black squares) is plotted as function of inverse stage. The dashed blue lines values in the figure depict the frequency softening by biaxial strain. The blue crosses depict the positions after subtracting this internal strain. The second y-scale depicts the C—C bond length owing a linear relation to the 2D line. The short red line are the experimental XRD bond length of the upper x-axes in (a).

broad doping range the charge transfer induced strain compensates the nonadiabatic effects. For this reason, we used the experimental position of the “pristine” G_C since we observe for all intercalation compounds a charge transfer to the charged layers above $4 \times 10^{13}/\text{cm}^{-2}$ (see Table 1). Interestingly, although one would expect a higher contribution of the charge transfer to the effective strain, adding the same effective biaxial strain as for the G_{UC} we find a nearly perfect match of the resulting frequency (blue crosses) with the experimental G_C. This confirms that the G-line response in GIC is related to charged and strained graphene layers. We point out that this model cannot be directly applied for stage I and stage II GICs because there are no uncharged graphene layers, the charge transfer is much stronger and the line position is influenced by the Fano interference with the conduction electrons.^{31,55}

The same analysis performed to the second order 2D line (strongest component related to the main second order Raman process) is shown in Figure 4b. We observe a linear decrease in position of the main 2D line as function of the inverse stage (red circles). The vertical dashed blue lines again correspond to the strain induced downshift of pristine graphene. The blue labels in the figure correspond to the relative percentage of biaxial strain from ref 29 and the

evaluated downshift using the Grüneisen parameter for the 2D-line.⁸ Because of the higher frequency of the 2D line, a much bigger shift between 10 and 40 cm⁻¹ is observed. The upshift due to the residual weak charging can be estimated to be less than 2 cm⁻¹ (ref 5) and can be neglected. Therefore, we are able to artificially “release” the biaxial strain and compare the 2D-line in “unstrained” KC₃₆, KC₄₈, KC₆₀, and KC₇₂ (blue crosses in Figure 4b) to the experimental position of unstrained mono-, bi-, tri-, and quad-layer graphene from ref 5 (black squares in Figure 4b). We find a very good agreement. This confirms that the 2D-line in GIC comes from strained multilayer graphene.

In addition, we can go one step further and compare the 2D line position to absolute in-plane lattice constants of the graphene layers based on the XRD results. This relies on the fact that Nixon and Perry²⁹ observed a linear relation of the in plane lattice constant versus inverse stage of the GIC. This allows to use the measured lattice constants to accurately correlate the 2D frequency to the C—C bond length shown as the right y-axes of Figure 4 b). Thus, one can use the 2D Raman response directly to determine the in-plane lattice constant of mono- and multilayer graphene as a function of their internal strain even on an absolute scale. This demonstrates that Raman spectroscopy is a very powerful tool to identify local internal strain in

single and few-layer graphene and their nanoelectronic devices and composites, yielding even absolute in plane lattice constants.

CONCLUSIONS

In summary, we have analyzed the intrinsic Raman response from strained graphene layers in graphite intercalation compounds. For stage III and higher there are two nearest layer environments: heavily charged graphene layers adjacent to an intercalant layer and basically uncharged graphene layers sandwiched between other graphene layers. By *ab initio* calculations of the charge densities and the electronic band dispersions, we have demonstrated that the charge transfer is incomplete (less than 1 electron per potassium atom) and that most (but not all) of the transferred charge remains on the charged graphene layers adjacent to the intercalants. This leads to an electronic decoupling of the inner (uncharged) from the outer (charged) layers and consequently also to a decoupling

of the corresponding Raman spectra: The G-line splits into two peaks, and the 2D line is entirely due to the uncharged inner layers while the 2D line of the outer layers is suppressed due to the strong charging. The quantitative interpretation of the peak positions requires that the internal strain of the graphene layers is taken into account. This allows us to unambiguously identify the Raman response of strained charged and uncharged graphene layers and to correlate it to the in-plane lattice constant determined by XRD. This highlights that Raman spectroscopy as contact free method has the potential to set the standard to determine the absolute local strain in graphene nanostructures. This covers uncharged and weakly charged single and few-layer graphenes and carbon nanotubes even in cases where no XRD results are available. For instance, this allows identifying the strain in nanocarbon based nanoelectronic and optoelectronic devices as well as the local interfacial strain in graphene and carbon nanotube polymer composites on an absolute scale.

MATERIALS AND METHODS

The intercalation experiments on natural graphite single crystals have been conducted *in situ* in a vacuum of more than $\sim 4 \times 10^{-8}$ mbar keeping the graphite sample inside a quartz ampule with a flat surface. The Raman measurements have been performed using 458, 488, 514, 568, and 647 nm excitation wavelengths at 1.2 mW between 1400 and 3000 cm^{-1} . Potassium with a 99.95% purity (Aldrich) was evaporated until bright golden graphite crystals which are assigned to stage I KC_8 were obtained.⁵⁵ Subsequently, the sample was resistively heated to 200 °C until it turned homogeneously blue (characteristic color of stage II KC_{24}). A controlled *in situ* high vacuum high temperature deintercalation process was performed by increasing the temperature in steps of 50 °C.¹⁴ The line positions were corrected by employing calibration lamps. Six potassium GIC stage I to VI (KC_8 , KC_{24} , KC_{36} , KC_{48} , KC_{60} , and KC_{72}) were identified for all laser lines used. Once each stage was identified, we followed a protocol acquiring multifrequency Raman spectra keeping constant the acquisition region, and maintaining the lowest possible exposure time to avoid laser-induced deintercalation as, for instance, reported by Guerard⁵⁶ and later on by us.⁵⁵

The calculation of electronic band structures and charge densities were performed using density-functional theory in the local density approximation. We have used the code **quantum-espresso**.⁵⁷ For the values of the K–C and C–C interplane distances as well as for the in-plane lattice constants, we used the experimental values given in Table 4 of ref 14; i.e., $a = 1.42$ Å for the bond-length, $d = 3.35$ Å for the interplane distance in graphite, and $d_M = 5.41$ Å for the distance between the intercalated layers. For simplicity, in order to keep supercell size low, we used AA stacking in adjacent graphene layers, except for KC_{36} where we used ABA stacking. K atoms were placed between the centers of carbon hexagons. No geometry relaxation was undertaken. The reciprocal unit-cell was sampled by a $6 \times 6 \times 2$ Monkhorst–Pack grid. Norm-conserving pseudopotentials (with nonlinear core correction for K) and an energy cutoff at 60 Ry were used. (For the phonon calculations, we used a “simplified” third-stage GIC: KC_{36} where each of the three graphene layers contains eight carbon atoms per unit cell. The K/C ratio is a factor 1.5 higher than in KC_{24} . We thus probe the influence of intercalation on the phonon frequencies under rather more severe conditions. The phonons are calculated using density-functional perturbation theory as

implemented in the quantum-espresso code. The in-plane and perpendicular lattice constants are the same as in the charge-density and band-structure calculations. We use a $15 \times 15 \times 4$ k-point sampling for the GIC and $15 \times 15 \times 1$ sampling for the isolated layer. A thermal (Gaussian) smearing of 0.02 Ry is applied to the occupation of the electronic bands.)

Conflict of Interest: The authors declare no competing financial interest.

Acknowledgment. We acknowledge financial support of the project through FWF-I377-N16, the OEAD AMADEUS PROGRAM financing. L.W. acknowledges funding by the ANR (French National Research Agency) through project ANR-09-BLAN-0421-01. Calculations were done at the IDRIS supercomputing center, Orsay (Project No. 091827) and at the Tirant Supercomputer of the University of Valencia (group vlc44).

Supporting Information Available: Raman spectra from stage III to stage VI potassium GIC are presented. The different spectra acquired using laser-excitation wavelengths in the range of (458 and 647 nm) are shown, as well as the intensity ratio (*R*) of the two G line components as function of stage at different photon energies. This material is available free of charge via the Internet at <http://pubs.acs.org>.

REFERENCES AND NOTES

- Ferrari, A. C.; Meyer, J. C.; Scardaci, V.; Casiraghi, C.; Lazzeri, M.; Mauri, F.; Piscanec, S.; Jiang, D.; Novoselov, K. S.; Roth, S.; et al. Raman Spectrum of Graphene and Graphene Layers. *Phys. Rev. Lett.* **2006**, *97*, 187401–4.
- Ferrari, A. C. Raman Spectroscopy of Graphene and Graphite: Disorder, Electron-Phonon Coupling, Doping and Nonadiabatic Effects. *Solid State Commun.* **2007**, *143*, 47–57.
- Malard, L. M.; Pimenta, M. A.; Dresselhaus, G.; Dresselhaus, M. S. Raman Spectroscopy in Graphene. *Phys. Rep.* **2009**, *473*, 51–87.
- Saito, R.; Hofmann, M.; Dresselhaus, G.; Jorio, A.; Dresselhaus, M. S. Raman Spectroscopy of Graphene and Carbon Nanotubes. *Adv. Phys.* **2011**, *60*, 413–550.
- Graf, D.; Molitor, F.; Ensslin, K.; Stampfer, C.; Jungen, A.; Hierold, C.; Wirtz, L. Spatially Resolved Raman Spectroscopy

- of Single- and Few-Layer Graphene. *Nano Lett.* **2007**, *7*, 238–242.
6. Mohiuddin, T. M. G.; Lombardo, A.; Nair, R. R.; Bonetti, A.; Savini, G.; Jalil, R.; Bonini, N.; Basko, D. M.; Galotis, C.; Marzari, N.; et al. Uniaxial Strain in Graphene by Raman Spectroscopy: G Peak Splitting, Grüneisen Parameters, and Sample Orientation. *Phys. Rev. B* **2009**, *79*, 205433–8.
 7. Huang, M.; Yan, H.; Chen, C.; Song, D.; Heinz, T. F.; Hone, J. Phonon Softening and Crystallographic Orientation of Strained Graphene Studied by Raman Spectroscopy. *Proc. Natl. Acad. Sci. U.S.A.* **2009**, *106*, 7304–7308.
 8. Metzger, C.; Remi, S.; Liu, M.; Kusminskiy, S. V.; Castro Neto, A. H.; Swan, A. K.; Goldberg, B. B. Biaxial Strain in Graphene Adhered to Shallow Depressions. *Nano Lett.* **2010**, *10*, 6–10.
 9. Frank, O.; Mohr, M.; Maultzsch, J.; Thomsen, C.; Riaz, I.; Jalil, R.; Novoselov, K. S.; Tsoukleri, G.; Parthenios, J.; Papagelis, K.; et al. Raman 2D-Band Splitting in Graphene: Theory and Experiment. *ACS Nano* **2011**, *5*, 2231–2239.
 10. Malard, L. M.; Nilsson, J.; Elias, D. C.; Brant, J. C.; Plentz, F.; Alves, E. S.; Castro Neto, A. H.; Pimenta, M. A. Probing the Electronic Structure of Bilayer Graphene by Raman Scattering. *Phys. Rev. B* **2007**, *76*, 201401–4.
 11. Yan, J.; Zhang, Y. B.; Kim, P.; Pinczuk, A. Electric Field Effect Tuning of Electron-Phonon Coupling in Graphene. *Phys. Rev. Lett.* **2007**, *98*, 166802–4.
 12. Casiraghi, C.; Pisana, S.; Novoselov, K. S.; Geim, A. K.; Ferrari, A. C. Raman Fingerprint of Charged Impurities in Graphene. *Appl. Phys. Lett.* **2007**, *91*, 233108–3.
 13. Stampfer, C.; Molitor, F.; Graf, D.; Ensslin, K.; Jungen, A.; Hierold, C.; Wirtz, L. Raman Imaging of Doping Domains in Graphene on SiO₂. *Appl. Phys. Lett.* **2007**, *91*, 241907–3.
 14. Dresselhaus, M. S.; Dresselhaus, G. Intercalation Compounds of Graphite. *Adv. Phys.* **2002**, *51*, 1–186.
 15. Doll, G. L.; Eklund, P. C.; Fischer, J. E. Raman-scattering Study of the High-frequency Graphitic Intralayer Modes in Li-graphite and the Stage Dependence of the Mode Frequency in Donor Graphite-Intercalation Compounds. *Phys. Rev. B* **1987**, *36*, 4940–4945.
 16. Yang, M. H.; Eklund, P. C. Optical Dielectric Function of High-Stage Potassium Graphite-Intercalation Compounds: Experiment and Theory. *Phys. Rev. B* **1988**, *38*, 3505–3516.
 17. Howard, C. A.; Dean, M. P. M.; Withers, F. Phonons in Potassium-Doped Graphene: The Effects of Electron-Phonon Interactions, Dimensionality, and Adatom Ordering. *Phys. Rev. B* **2011**, *84*, 241404–4.
 18. Emery, N.; Herold, C.; d'Astuto, M.; Garcia, V.; Bellin, C.; Mareche, J. F.; Lagrange, P.; Loupiaz, G. Superconductivity of Bulk CaC₆. *Phys. Rev. Lett.* **2005**, *95*, 087003–4.
 19. Weller, T. E.; Ellerby, M.; Saxena, S. S.; Smith, R. P.; Skipper, N. T. Superconductivity in the Intercalated Graphite Compounds C₆Yb and C₆Ca. *Nat. Phys.* **2005**, *1*, 39–41.
 20. Zhao, W.; Tan, P. H.; Liu, J.; Ferrari, A. C. Intercalation of Few-Layer Graphite Flakes with FeCl₃: Raman Determination of Fermi Level, Layer by Layer Decoupling, and Stability. *J. Am. Chem. Soc.* **2011**, *133*, 5941–5946.
 21. Dimiev, A. M.; Ceriotti, G.; Behabtu, N.; Zakhidov, D.; Pasquali, M.; Saito, R.; Tour, J. M. Direct Real-Time Monitoring of Stage Transitions in Graphite Intercalation Compounds. *ACS Nano* **2013**, *7*, 2773–2780.
 22. McGovern, I. T.; Eberhardt, W.; Plummer, E. W.; Fischer, J. E. Band Structures of Graphite and Graphite-Intercalation Compounds as Determined by Angle Resolved Photoemission Using Synchrotron Radiation. *Physica B+C* **1980**, *99*, 415–419.
 23. Lagues, M.; Fischer, J. E.; Marchand, D.; Fretigny, C. Angle Resolved Photoemission Spectroscopy of CsC₈ - Evidence for a Charge-Density Wave Localized at the Surface. *Solid State Commun.* **1988**, *67*, 1011–1015.
 24. Grueneis, A.; Attacalite, C.; Rubio, A.; Vyalikh, D. V.; Molodtsov, S. L.; Fink, J.; Follath, R.; Eberhardt, W.; Buechner, B.; Pichler, T. Angle-Resolved Photoemission Study of the Graphite Intercalation Compound KC₈: A Key to Graphene. *Phys. Rev. B* **2009**, *80*, 075431–5.
 25. Grueneis, A.; Attacalite, C.; Rubio, A.; Vyalikh, D. V.; Molodtsov, S. L.; Fink, J.; Follath, R.; Eberhardt, W.; Buechner, B.; Pichler, T. Electronic Structure and Electron-Phonon Coupling of Doped Graphene Layers in KC₈. *Phys. Rev. B* **2009**, *79*, 205106–9.
 26. Ohno, T.; Kamimura, H. Band Structures and Charge-Distributions Along the C-Axis of Higher Stage Graphite-Intercalation Compounds. *J. Phys. Soc. Jpn.* **1983**, *52*, 223–232.
 27. Blinowski, J.; Hau, N. H.; Rigaux, C.; Vieren, J. P.; Letoullec, R.; Furdin, G.; Herold, A.; Melin, J. Band-Structure Model and Dynamical Dielectric Function in Lowest Stages of Graphite Acceptor Compounds. *J. Phys. (Paris)* **1980**, *41*, 47–58.
 28. Saito, R.; Kamimura, H. Orbital Susceptibility of Higher Stage GlCs. *Synth. Met.* **1985**, *12*, 295–300.
 29. Nixon, D. E.; Parry, G. S. Expansion of Carbon-Carbon Bond Length in Potassium Graphites. *J. Phys. C: Solid State Phys.* **1969**, *2*, 1732–1741.
 30. Solin, S. A. Raman and IR Studies of Graphite Intercalates. *Physica* **1980**, *99B*, 443–452.
 31. Solin, S. A.; Caswell, N. Raman-Scattering from Alkali Graphite-Intercalation Compounds. *J. Raman Spectrosc.* **1981**, *10*, 129–135.
 32. Pisana, S.; Lazzeri, M.; Casiraghi, C.; Novoselov, K. S.; Geim, A. K.; Ferrari, A. C.; Mauri, F. Breakdown of the Adiabatic Born-Oppenheimer Approximation in Graphene. *Nat. Mater.* **2007**, *6*, 198–201.
 33. Saitta, A. M.; Lazzeri, M.; Calandra, M.; Mauri, F. Giant Nonadiabatic Effects in Layer Metals: Raman Spectra of Intercalated Graphite Explained. *Phys. Rev. Lett.* **2008**, *100*, 226401–4.
 34. Wang, Y. Y.; Ni, Z. H.; Yu, T.; Shen, Z. X.; Wang, H. M.; Wu, Y. H.; Chen, W.; Wee, A. T. S. Raman Studies of Monolayer Graphene: The Substrate Effect. *J. Phys. Chem. C* **2008**, *112*, 10637–10640.
 35. Doll, G. L.; Yang, M. H.; Eklund, P. C. Comparative Optical Study of the Two-Dimensional Donor-Type Intercalation Compounds Graphite-KH_x and Their Binary Counterparts C₈K and C₂₄K. *Phys. Rev. B* **1987**, *35*, 9790–9798.
 36. Vidano, R. P.; Fischbach, D. B.; Willis, L. J.; Loehr, T. M. Observation of Raman Band Shifting with Excitation Wavelength for Carbons and Graphites. *Solid State Commun.* **1981**, *39*, 341–344.
 37. Venezuela, P.; Lazzeri, M.; Mauri, F. Theory of Double-Resonant Raman Spectra in Graphene: Intensity and Line Shape of Defect-Induced and Two-Phonon Bands. *Phys. Rev. B* **2011**, *84*, 035433–25.
 38. Malard, L. M.; Guimaraes, M. H. D.; Mafra, D. L.; Mazzoni, M. S. C.; Jorio, A. Group-Theory Analysis of Electrons and Phonons in N-Layer Graphene Systems. *Phys. Rev. B* **2009**, *79*, 125426–8.
 39. Hartwigsen, C.; Witschel, W.; Spohr, E. Charge Density and Charge Transfer in Stage-1 Alkali-Graphite Intercalation Compounds. *Phys. Rev. B* **1997**, *55*, 4953–4959.
 40. Ancilotto, F.; Toigo, F. 1st Principles Study of Potassium Adsorption on Graphite. *Phys. Rev. B* **1993**, *47*, 13713–13721.
 41. Das, A.; Pisana, S.; Chakraborty, B.; Piscanec, S.; Saha, S. K.; Waghmare, U. V.; Novoselov, K. S.; Krishnamurthy, H. R.; Geim, A. K.; Ferrari, A. C.; et al. Monitoring Dopants by Raman Scattering in an Electrochemically Top-Gated Graphene Transistor. *Nanotechnol.* **2008**, *3*, 210–215.
 42. Lazzeri, M.; Mauri, F. Nonadiabatic Kohn Anomaly in a Doped Graphene Monolayer. *Phys. Rev. Lett.* **2006**, *97*, 266407–4.
 43. Thomsen, C.; Reich, S. Double Resonant Raman Scattering in Graphite. *Phys. Rev. Lett.* **2000**, *85*, 5214–5217.
 44. Lazzeri, M.; Attacalite, C.; Wirtz, L.; Mauri, F. Impact of the Electron-Electron Correlation on Phonon Dispersion: Failure of LDA and GGA DFT Functionals in Graphene and Graphite. *Phys. Rev. B* **2008**, *78*, 081406–4.
 45. Ziegler, D.; Gava, P.; Guettinger, J.; Molitor, F.; Wirtz, L.; Lazzeri, M.; Saitta, A. M.; Stemmer, A.; Mauri, F.; Stampfer, C. Variations in the Work Function of Doped Single- and

- Few-Layer Graphene Assessed by Kelvin Probe Force Microscopy and Density Functional Theory. *Phys. Rev. B* **2011**, *83*, 235434–7.
46. Grueneis, A.; Attacalite, C.; Pichler, T.; Zabolotnyy, V.; Shiozawa, H.; Molodtsov, S. L.; Inosov, D.; Koitzsch, A.; Knupfer, M.; Schiessling, J.; et al. Electron-Electron Correlation in Graphite: A Combined Angle-Resolved Photoemission and First-Principles Study. *Phys. Rev. Lett.* **2008**, *100*, 037601–4.
 47. Piscanec, S.; Lazzeri, M.; Mauri, F.; Ferrari, A. C.; Robertson, J. Kohn Anomalies and Electron-Phonon Interactions in Graphite. *Phys. Rev. Lett.* **2004**, *93*, 185503–4.
 48. Attacalite, C.; Wirtz, L.; Lazzeri, M.; Mauri, F.; Rubio, A. Doped Graphene as Tunable Electron-Phonon Coupling Material. *Nano Lett.* **2010**, *10*, 1172–1176.
 49. Allard, A.; Wirtz, L. Graphene on Metallic Substrates: Suppression of the Kohn Anomalies in the Phonon Dispersion. *Nano Lett.* **2010**, *10*, 4335–4340.
 50. Forster, F.; Molina-Sánchez, A.; Engels, S.; Epping, A.; Watanabe, K.; Taniguchi, T.; Wirtz, L.; Stampfer, C. Dielectric Screening of the Kohn Anomaly of Graphene on Hexagonal Boron Nitride. *Phys. Rev. B* **2013**, *88*, 085419–7.
 51. Pietronero, L.; Strassler, S. Bond-Length Change as a Tool to Determine Charge-Transfer and Electron-Phonon Coupling in Graphite-Intercalation Compounds. *Phys. Rev. Lett.* **1981**, *47*, 593–596.
 52. Ishioka, K.; Hase, M.; Kitajima, M.; Wirtz, L.; Rubio, A.; Petek, H. Ultrafast Electron-Phonon Decoupling in Graphite. *Phys. Rev. B* **2008**, *77*, 121402(R)–4.
 53. Das, A.; Chakraborty, B.; Piscanec, S.; Pisana, S.; Sood, A. K.; Ferrari, A. C. Phonon Renormalization in Doped Bilayer Graphene. *Phys. Rev. B* **2009**, *79*, 155417–7.
 54. Parret, R.; Paillet, M.; Huntzinger, J.-R.; Nakabayashi, D.; Michel, T.; Tiberj, A.; Sauvajol, J.-L.; Zahab, A. A. *In-Situ* Raman Probing of Graphene Over a Broad Doping Range Upon Rubidium Vapor Exposure. *ACS Nano* **2013**, *7*, 165–173.
 55. Chacon-Torres, J. C.; Ganin, A. Y.; Rosseinsky, M. J.; Pichler, T. Raman Response of Stage-1 Graphite Intercalation Compounds Revisited. *Phys. Rev. B* **2012**, *86*, 075406–6.
 56. Nemanich, R. J.; Solin, S. A.; Guérard, D. Raman-Scattering from Intercalated Donor Compounds of Graphite. *Phys. Rev. B* **1977**, *16*, 2665–2672.
 57. Giannozzi, P.; Baroni, S.; Bonini, N.; Calandra, M.; Car, R.; Cavazzoni, C.; Ceresoli, D.; Chiarotti, G. L.; Cococcioni, M.; Dabo, I.; et al. QUANTUM ESPRESSO: a Modular and Open-Source Software Project for Quantum Simulations of Materials. *J. Phys.: Condens. Matter* **2009**, *21*, 395502–19.